



This is a repository copy of *Improved breakdown strength and energy storage density of a Ce doped strontium titanate core by silica shell coating*.

White Rose Research Online URL for this paper:
<http://eprints.whiterose.ac.uk/138447/>

Version: Accepted Version

Article:

Qi, J., Cao, M., Heath, J.P. et al. (5 more authors) (2018) Improved breakdown strength and energy storage density of a Ce doped strontium titanate core by silica shell coating. *Journal of Materials Chemistry C*, 6 (34). pp. 9130-9139. ISSN 2050-7526

<https://doi.org/10.1039/c8tc03181a>

© 2018 The Royal Society of Chemistry. This is an author produced version of a paper subsequently published in *Journal of Materials Chemistry C*. Uploaded in accordance with the publisher's self-archiving policy.

Reuse

Items deposited in White Rose Research Online are protected by copyright, with all rights reserved unless indicated otherwise. They may be downloaded and/or printed for private study, or other acts as permitted by national copyright laws. The publisher or other rights holders may allow further reproduction and re-use of the full text version. This is indicated by the licence information on the White Rose Research Online record for the item.

Takedown

If you consider content in White Rose Research Online to be in breach of UK law, please notify us by emailing eprints@whiterose.ac.uk including the URL of the record and the reason for the withdrawal request.



eprints@whiterose.ac.uk
<https://eprints.whiterose.ac.uk/>

Improved breakdown strength and energy storage density of Ce doped strontium titanate core by silica shell coating

Junlei Qi¹, Minghe Cao^{1*}, James P. Heath², Julian S. Dean², Hua Hao¹, Zhonghua

Yao¹, ZhiYong Yu¹ and Hanxing Liu³

¹State Key Laboratory of Advanced Technology for Materials Synthesis and Processing, Wuhan University of Technology, Wuhan 430070, Hubei, PR China,

² Department of Materials Science & Engineering, University of Sheffield, Sir Robert Hadfield Building, Mappin Street, Sheffield S1 3JD, UK

³ International School of Materials Science and Engineering, Wuhan University of Technology, Wuhan 430070, PR China.

Corresponding author: Minghe Cao E-mail address: caominghe@whut.edu.cn (M. Cao)

Abstract

For single phase dielectric ceramics made by traditional solid state preparation, the conflict between high dielectric permittivity and low breakdown strength has always limited the improvement of energy storage density. Here, we design a core-shell structure of $\text{Sr}_{0.985}\text{Ce}_{0.01}\text{TiO}_3$ (SCT) @xwt% SiO_2 combining a high dielectric permittivity core with an insulating shell material. The sample of x=3 wt% sintered at 1300 ° C has the largest energy storage density $\sim 2.23 \text{ J/cm}^3$. The effect that different amounts of SiO_2 has on phase, microstructure, dielectric and energy storage properties were investigated by X-ray diffraction (XRD), transmission electron microscopy (TEM), scanning electron microscopy with energy spectrum (SEM-EDS) and dielectric measurements. As verified by finite element simulations, the energy storage properties are mainly governed by the electric field distribution owing to the introduction of a high dielectric permittivity core (SCT) in the low permittivity shell. The shell material provides an electrical shielding effect around the core, resulting in a significant reduction in the field strength within the core material. Comparison of experimental and simulated results also shows good agreement for the breakdown properties.

Keywords

SCT@ SiO_2 ; core shell structure; dielectric properties; energy storage; finite element simulation.

Introduction

In order to meet the development goals for lightweight and miniaturized energy storage electronic components, higher requirements have been put forward for dielectric materials¹. The search for dielectric materials with high permittivity, low dielectric loss and high breakdown strength has always been the focus of researchers in the high energy density storage fields.^{2,3} Strontium titanate (SrTiO₃) has been widely applied in energy storage devices, electronics, microwave applications, dynamic random access memory (DRAM) and multi-layer capacitors because of its high permittivity and low dielectric loss^{4,5}. It is well known that doping can effectively improve the dielectric properties of materials, while the addition of rare earth elements can improve the dielectric permittivity and temperature stability⁶⁻⁸. However, the energy density does not only depend on permittivity but also breakdown strength⁹. For parallel capacitors, the energy density is dependent on the dielectric properties of the material that separates the opposite static charges between two electrodes, the total stored energy density U is given as follows:

$$U = \int E dP \quad (1)$$

Where E is applied electric field and P is the polarization. For linear dielectric, the energy density U is:

$$U = \frac{1}{2} \epsilon_r \epsilon_0 E^2 \quad (2)$$

where ϵ_r is the dielectric constant of the material, ϵ_0 is the vacuum permittivity^{10,11}. Therefore, good linear dielectric materials should possess high dielectric permittivity ϵ_r along with a high electric field, E to guarantee high storage energy density.

Multi-phase composites, combining materials with relatively high dielectric properties and high breakdown strength have been proposed as a method of achieving high energy density. They have been widely studied, such as BTO@TO nfs/P(VDF-HFP)¹², sandwich-structure BT/PVDF¹³, BT/PMMA¹⁴ etc. However, such organic/inorganic composite materials have limitations such as the inability to withstand high temperatures. Wu et al. reported BaTiO₃@SrTiO₃, that combining the ferroelectric BT and paraelectric ST, results in high polarization, however the high dielectric loss and low breakdown strength limits its application¹⁵. Silicon dioxide is considered to be a material with high electrical insulation and high temperature resistance. Recent studies have shown that with SiO₂ additives the breakdown strength is increased several times compared to a pure material with a reduction in the permittivity¹⁶. The addition of glass forms a secondary phase with the other substances that have a low melting point and therefore reduces the sintering temperature¹⁷⁻²⁰. Moreover, chemical coating methods have been shown to be more effective than conventional solid state additive reaction methods because the core shell structure can modify the surface of particles while maintaining a uniform shell layer²¹⁻²⁴.

It is well-known that rare element doping is an effective method to enhance

dielectric, piezoelectric²⁵ and multiferroic²⁶ properties. In our previous work, we synthesized $\text{Sr}_{0.985}\text{Ce}_{0.01}\text{TiO}_3$ (SCT) ceramics which possess high dielectric properties and stability over wide temperature range²⁷. Hence, we selected SCT particles as the core material. On the other hand, the intrinsic properties of SiO_2 also should merit attention, such as high breakdown strength, thermal stability and ease of surface-modification²⁸. Here, we studied the effects of different SiO_2 amounts (xwt%) on the phase, microstructure, morphology, dielectric properties and breakdown strength on SCT. Finite element simulation are used to analyze the composite electrical response as a function of SCT volume fraction for a fixed grain size. This allows us to simulate values of the key parameters for an energy storage device such as: permittivity, breakdown strength and energy storage density. These values were then compared to the experimental results to confirm the SCT volume fraction.

Experimental

Synthesis of SCT Particles.

The whole synthesis process is divided into two major parts (see fig. 1). The first part is producing Ce doped of strontium titanate powders (the core) via solid-state method. High-purity SrCO_3 (AR), TiO_2 (CP) and CeO_2 (99.99%) (Sinopharm Chemical Reagent Co., Ltd) were used as the starting materials. Stoichiometric amounts of powder mixtures were ball-milled in ethanol medium using yttria-stabilized zirconia balls in a plastic container for 48h. The slurry was dried, ground, sifted (325 mesh) and calcined at 1180°C . This process includes synthesis of Ce doped strontium titanate (SCT) of the main crystalline phase and the controlled grain size of synthetic powders. The powder was then ball-milled again, dried, ground and sifted (325 mesh).

Fabrication of SCT@ SiO_2 composites

The second part is coating SiO_2 shell layer with different amounts of tetraethoxysilane (TEOS) (1wt%, 3wt%, 5wt%, 7wt%) on pre-synthesized powders in order to form the core-shell structure. The SiO_2 -coated SCT process involved the following steps: Firstly, the SCT powders were dispersed in the 50ml absolute ethyl alcohol and adding glacial acetic acid ($\geq 99.5\%$) (Sinopharm Chemical Reagent Co., Ltd) and stirred in a water bath at 40°C for 1 hour, then ultrasonically dispersed for 1h. Secondly, TEOS was added to the mixed solution and treated with the same water bath condition, ammonia (25-28%) was added to control the pH to about 10. Finally, the SiO_2 -coated powders were dried.

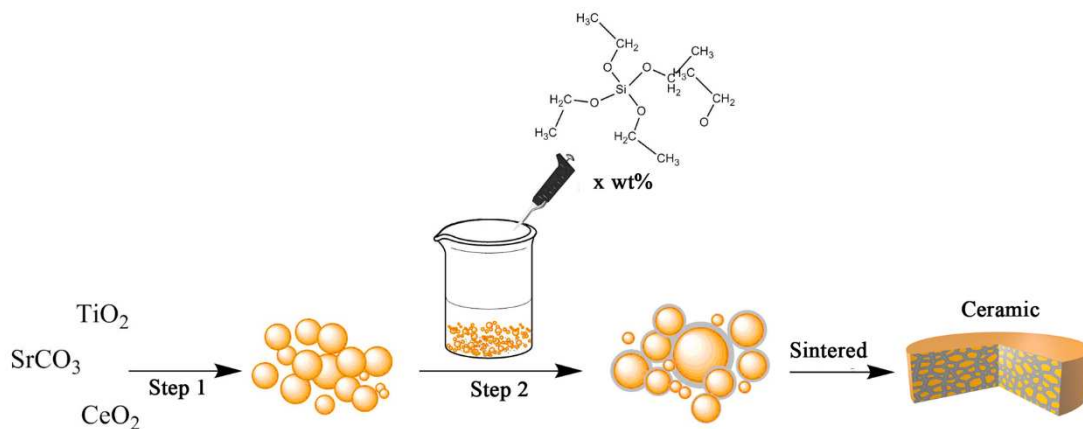


Figure 1. Processing route of experiment (Step 1 Ce doped STO powders synthesized by solid-state method, Step 2 Pre-doped powders were coated with various amounts of TEOS process via stober process.)

A solution of 4wt% poly (vinyl alcohol) 1799 (PVA) (alcoholysis 99.8~100% (mol/mol), Aladdin Industrial Co.) was added dropwise to the dried powders. Cylindrical pellets with a height of 1~2 mm and a diameter of 12mm were made applying a pressure of 120MPa. These compacts were then heated to 600°C to burn the binder out before sintering. Pellets were sintering at 1180~1480°C for 3h in a platinum crucible. For completeness, we also show experimental results of samples for pure SrTiO_3 (STO) coating with the 3wt% SiO_2 .

Characterization

The crystalline structure of sintered samples was analyzed by an X-ray diffractometer (XRD), using $\text{Cu-K}\alpha$ radiation (Bruker AXS D8 Advance). The microstructure and morphology of samples were examined by FE-TEM (JEOL JEM-2100F) and SEM-EDS (JEOL JSM-6700F). For electrical measurements, the sintered ceramic pellet was polished and coated with silver electrodes on both sides. The dielectric properties were measured by a precision impedance analyzer (Agilent 4980A) and the breakdown strength and P-E loops were measured by dielectric breakdown test system (PolyK technologies, PK-CPE1701) at room temperature. In addition, all the samples used for breakdown measurement were bulk ceramics (with pellet thickness of ~0.2mm).

Finite element simulation

The finite element modeling (FEM) code used in this study is capable of solving the electrical response of an arbitrary ceramic microstructure for a given applied voltage (AC or DC). Different regions of the model's geometry can be assigned their own values of conductivity and permittivity allowing the differentiation between core and shell material. A more rigorous presentation of mathematics and assumptions behind the model has been presented here²⁹. This technique has been used previously to simulate the impedance response of core-shell structures³⁰, interfaces effects in lamellar devices and temperature stable capacitance bi-layers^{31,32}.

To replicate the polycrystalline core-shell microstructure of SCT@SiO₂, first a granular structure was generated using Voronoi tessellation³³. A degree of randomness can be applied to the shape and size of the Voronoi grains whilst maintaining a distribution of allowed grain sizes. Experimentally the size of each grain is determined by averaging the value of the horizontal and vertical lines through the centroids of the grains. The distribution of grain sizes of the 3wt% SiO₂ composition is about 1~5 μm and the average grain is about 3μm. Taking the possible statistical error into consideration, the mean grain size of the model was set to ~4.5 μm. Core-shell structures were generated with a method used previously²⁹. In this work core volume fractions of 0.7 to 0.985 were simulated. The complete geometry of the simulations consisted of a 25 μm long cube containing 341 core-shell grains. As there was a degree of randomness in the microstructural configuration each simulation was repeated three times and the results averaged.

Once meshed, the core and shell regions are assigned conductivity and permittivity values. These were obtained experimentally by fabricating the core and shell regions in isolation. The core (SCT) and shell (Sr₂TiSi₂O₈) were synthesized via solid phase method by appropriate stoichiometry. The electrical properties of core and shell were measured by the same dielectric and ferroelectric test system. From the experimental results the conductivities of the core and shell regions were 8.6E-7 Sm⁻¹ and 3.9E-8 Sm⁻¹ respectively. The core and shell relative permittivities were ~678 and ~15 respectively.

To find the effective permittivity of the composite models a 100Hz 1 mV AC voltage was applied using boundary conditions. The resulting impedance could then be calculated from the current and voltage sinusoids. The impedance (Z^*) was then converted into a complex capacitance ($E^*=1/j\omega Z^*$), where j is the square root of minus one and ω is the angular frequency³⁴. E^* was then converted into a capacitance by dividing by the cube length times the permittivity of free space. This was repeated for all volume fractions.

Ideally the breakdown strength would be calculated by modelling the dynamic processes occurring during the breakdown event. Numerical methods capable of doing this exist, such as phase field modelling³⁵, but are computationally expensive and sometimes involve reducing the problem to two spatial dimensions to reduce the complexity. Here we opted for a different method, simply to simulate the electric field within our model and compare the electric field distribution to the value expected in a homogenous material (the applied field) to calculate the possible bounds of the breakdown strength, this was successfully used to predict the effect on breakdown strength arising from porosity³⁶. We simulate a 25 μm long cube with an applied DC voltage. If the simulation geometry was electrically homogenous there would be a homogenous electric field within the cube. We now consider a simulation geometry with a core-shell microstructure where the electrical properties of the core and shell differ. The electric field will then no longer be homogenous.

To find the bounds of the shell material's breakdown strength, first the electric field distribution in the shell was extracted from the simulation. If the maximum and minimum field strength in the shell were double and half that in the homogenous case

respectively it can be said the upper bound of the shell's effective breakdown is twice the normal value and the lower bound is halved. Dividing the breakdown strength by the intensification or minimization factor gives the lower or upper bounds of the predicted breakdown strength respectively. A comparison of these bounds with the experimental data is given in the FEM results section.

This approach requires the breakdown strength of the core and shell material to be known in advance. The breakdown strength core (SCT) and shell ($\text{Sr}_2\text{TiSi}_2\text{O}_8$) were measured by the dielectric breakdown test system (PolyK technologies, PK-CPE1701) using DC at room temperature. Should the predicted breakdown strength and permittivity match the experimental values a value of energy density can be calculated using equation (2).

Results and discussion

Morphologies of core-shell structure

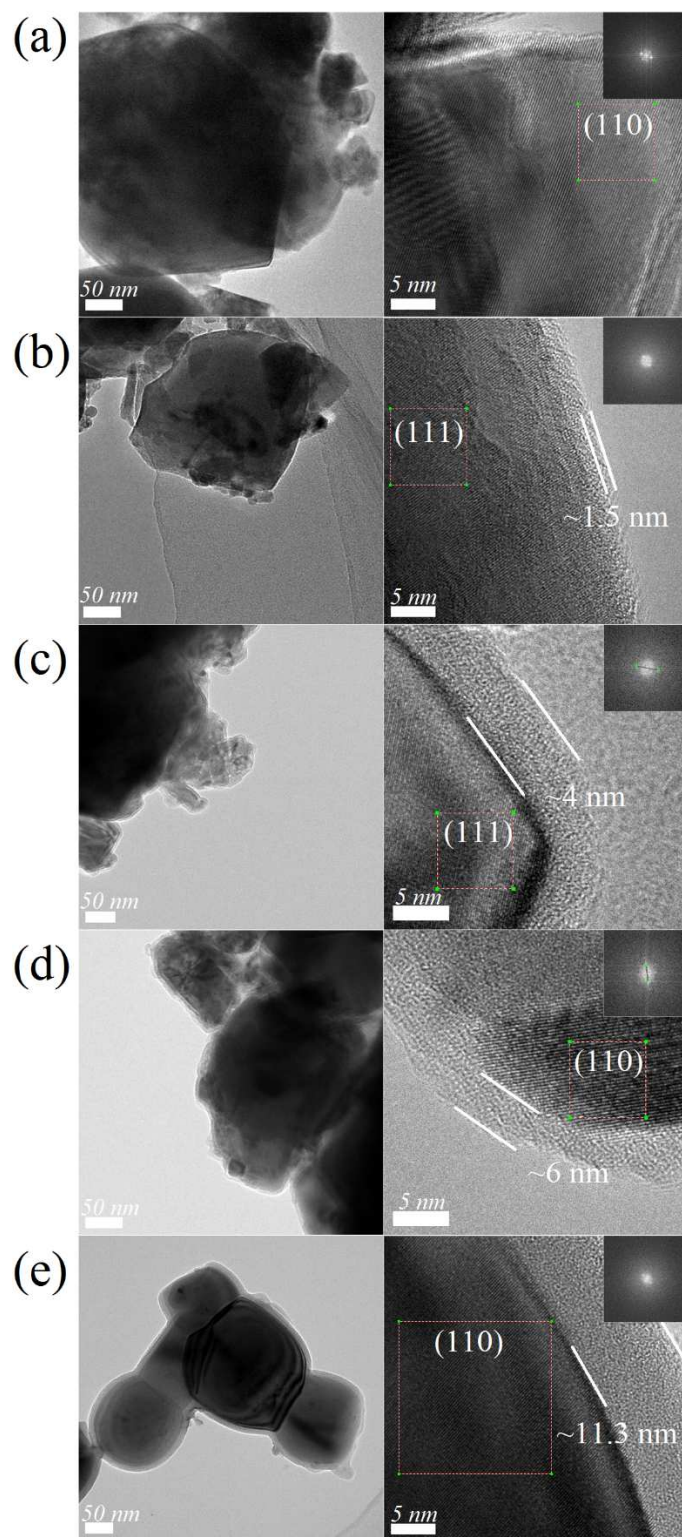


Figure 2. FE-TEM images for (a) uncoated SCT particles, (b) SCT@1.0wt% SiO₂, (c) SCT@3.0wt% SiO₂, (d) SCT@5.0wt% SiO₂ and (e) SCT@7.0wt% SiO₂. The insert figure shows a FFT for the highlighted selected area.

Figure 2 shows the FE-TEM images of SCT @ xwt % SiO₂ (x=0.0, 1.0, 3.0 5.0, 7.0) particles. The images show that the particles have a uniformly spherical morphology. Fast Fourier transform (FFT) was conducted to analyse the lattice fringe in the selected area and the indices of the crystal faces are marked in the inserted figures. Through the symmetry, after post-processing with FFT, it can be seen that the SCT crystals grow regularly and have high symmetry. The thickness of the SiO₂ coating layers range from about 1.5 nm to 11.3 nm (x= 1.0, 3.0, 5.0, 7.0 wt %). As clearly evidenced in these pictures, the radius of SCT@SiO₂ particles is about 200 nm and the SCT core are fully covered by SiO₂ coating layer, even at sharp edges. Although there is polydispersity in size and sharpness of the SCT particles, all of them were surrounded entirely by the same silica shell thickness. The thickness of xwt% SiO₂ (x=0.0, 1.0, 3.0, 5.0, 7.0) shell layer are shown in the Table 1.

Table 1. Thickness of SCT@xwt% SiO₂ shell layer.

x wt% SiO ₂	1.0 wt%	3.0 wt%	5.0 wt%	7 wt%
Shell thickness (nm)	1.5	4	6	11.3

Structure and microstructure of SCT@xwt% SiO₂ ceramics

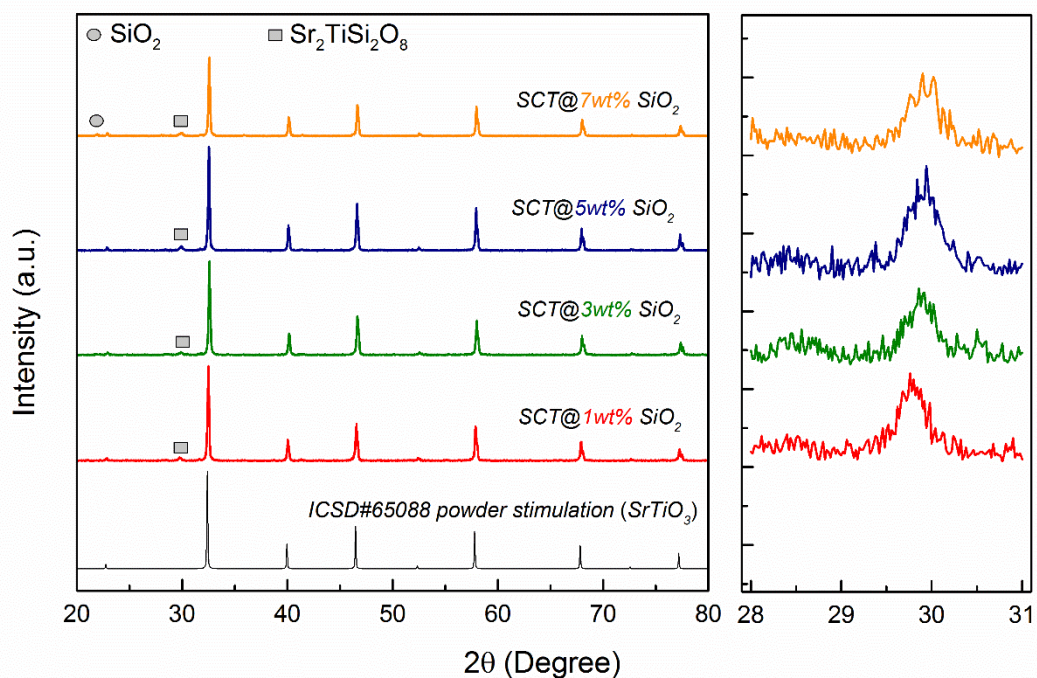
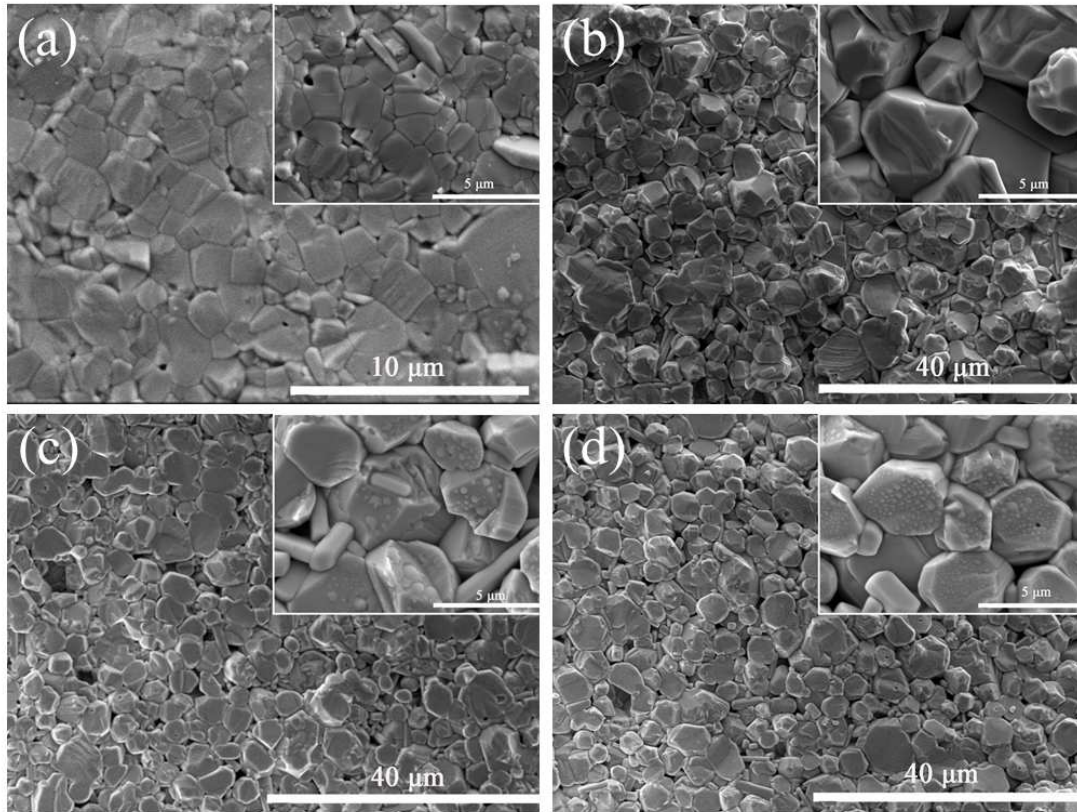


Figure 3. XRD patterns of SCT@xwt% SiO₂ ceramics (x=1.0, 3.0, 5.0, 7.0) sintered at 1280°C. Magnification of the patterns is from 28° to 31°.

The room temperature XRD patterns of SCT@xwt%SiO₂ (x=0, 1.0, 3.0, 5.0, 7.0, 20.0, 40.0) ceramics are shown in Figure 3. It can be seen that the doping and coating process did not change the structure of main crystal phase. All samples remain as a cubic perovskite structure and most likely space group is $Pm\bar{3}m$ ^{37, 38}. A magnified region of 28 to 31 degrees is shown as insert. This highlights a secondary peak of a Sr₂TiSi₂O₈ phase approximately 29.5 degrees. With increasing coating content, the peak become stronger and broader, with the diffraction peak

shifted to a higher angle. The same phenomenon also has been reported by Zhang et al.³⁹. This is owing to the appearance of interface reactions between these core and shell, which formed Sr-Ti-Si-O compounds during the sintering process. When the SiO₂ coating amount is greater than 5wt%, the diffraction peak of impurity phases SiO₂ become more intense. In other words, when the coating amount exceeds 5wt%, part of silica may not be completely coated on the cores surface but present as other phases in the samples.



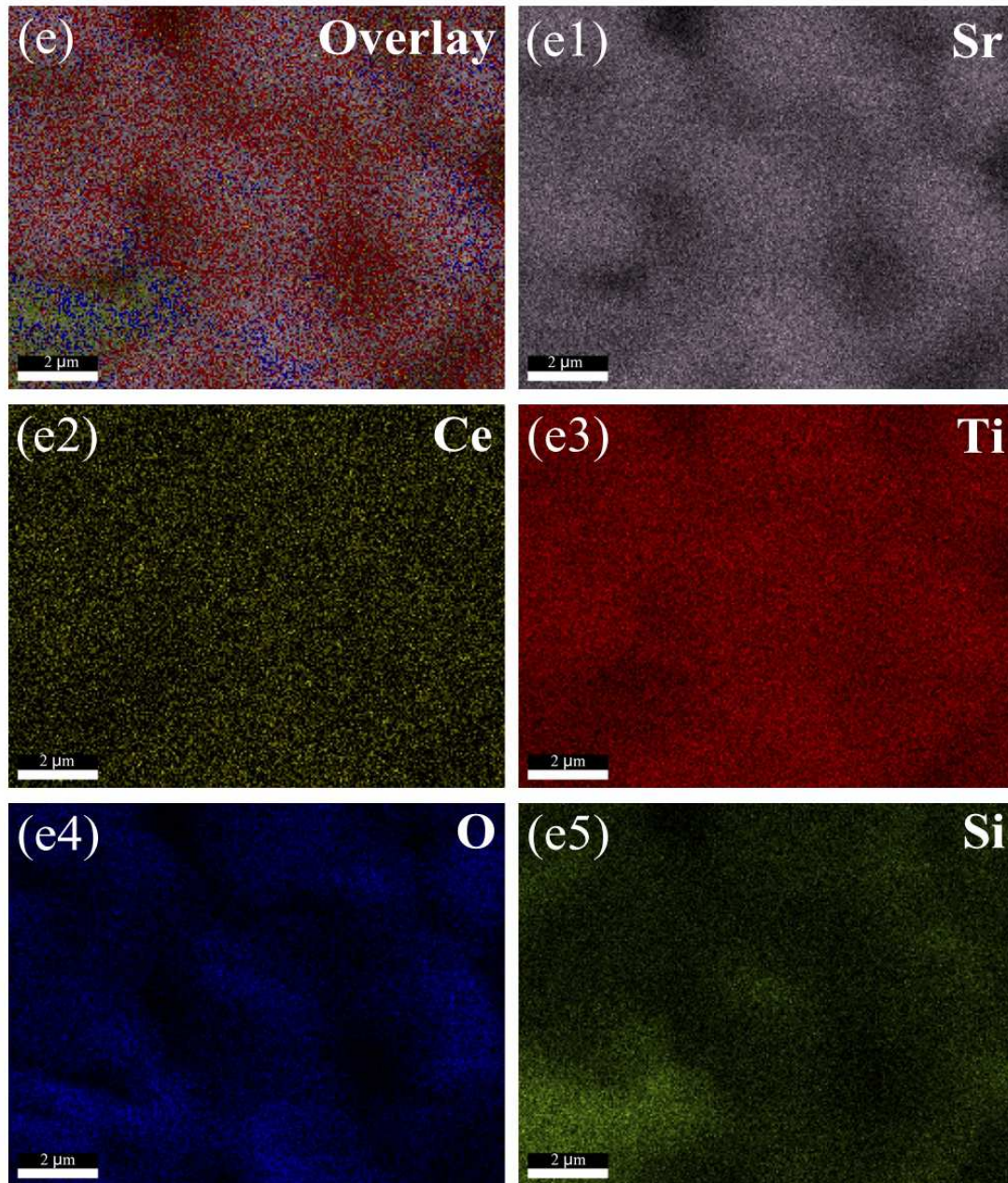


Figure 4. SEM pattern for the SCT@xwt% ceramics coated with various amounts of SiO₂ (a) 1.0wt% (b) 3.0wt% (c) 5.0wt% (d) 7.0wt% and (e) element overlay images for EDS of SCT@5wt% SiO₂ ceramic, grey for strontium (e1), yellow for cerium (e2), red for titanium (e3), blue for oxygen (e4), and green for silicon (e5), respectively.

Table 2. Average grain size of SCT@xwt% SiO₂ ceramics.

x wt% SiO ₂	1.0 wt%	3.0 wt%	5.0 wt%	7 wt%
Average grain size	1.36 μm	3.22 μm	3.85 μm	4.02 μm
(deviation)	(0.03)	(0.16)	(0.47)	(0.04)

Figure (4a) to (4d) shows the SEM images of fractured cross sections for SCT@ various coating amounts of xwt% (x=1.0, 3.0, 5.0, 7.0) SiO₂ ceramic samples. EDS results for ceramics of SCT@5wt% SiO₂ are shown in Figure 4e with individual plots of Sr (e1), Ce (e2), Ti (e3), O (e4) and Si (e5) highlighted separately. The grain size

of 1wt%, 3wt%, 5wt%, 7wt% SiO₂ is about 1.36 μm, 3.22 μm, 3.85 μm and 4.02 μm respectively, as shown in Table 2. It appears that with increasing amount of SiO₂, the grain size in the samples also increases. Compared with pure SCT (about 12~42 μm)²⁷, the introduction of silica contributes to fine crystallization and can effectively reduce the influence on breakdown strength of defects, such as pores, that are formed during the sintering process. Figure (e1- e3) shows that there is a uniform distribution of SCT (core) and Si (e5) and O (e4) elements with high concentration are present at the grain boundaries after sintering. The uniform distribution of Ce demonstrates that the shell layers of SiO₂ do not affect the main crystal structure and phase of SCT after sintering. The segregation of Si and O elements in the grain boundary indicates that the core-shell structure still maintains an independent phase, which is reflected in XRD results. When the coating amount exceeds 5wt%, there is an additional occurrence of the silica phase.

Dielectric properties of SCT@SiO₂ ceramics

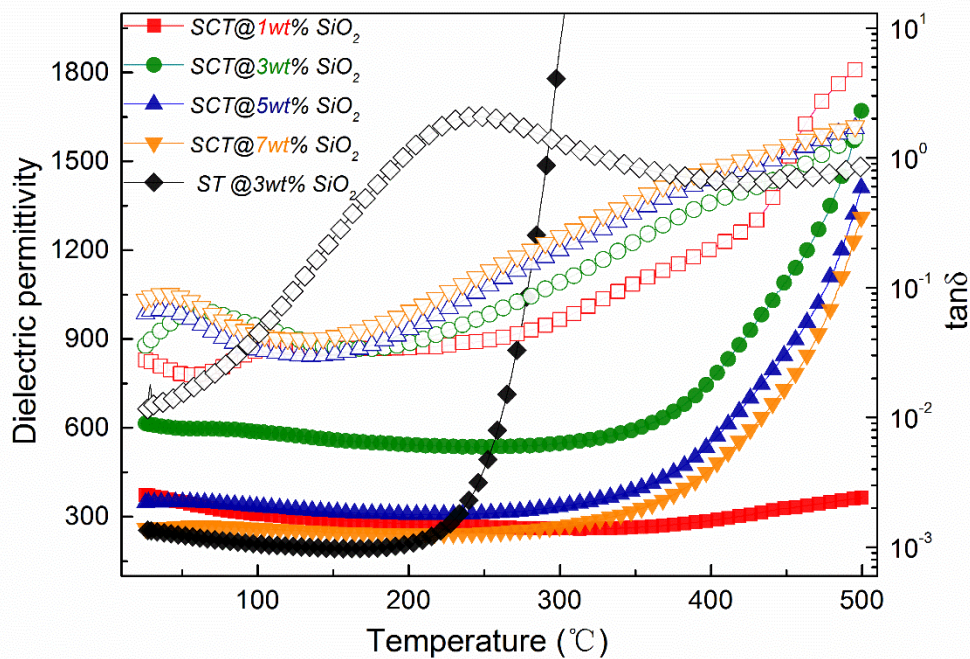


Figure 5. Temperature dependence of dielectric permittivity and loss for SCT@xwt% SiO₂ (x=1.0 (pink squares), 3.0 (green circles), 5.0 (blue upward pointing-triangles), 7.0 (orange downward pointing-triangles)) and ST@3wt% SiO₂ (black diamonds). All samples were sintered at 1300°C. Solid symbols for dielectric permittivity (right Y axis) and hollow symbols for dielectric loss (left Y axis).

Fig. 5 shows the temperature dependence of the dielectric permittivity and loss of SCT@xwt% SiO₂ and ST@3wt% SiO₂ ceramics at 1k Hz from room temperature to 500°C. The SCT@3wt% SiO₂ component has the highest dielectric constant ($\epsilon_r \sim 615$ at room temperature and 1 kHz) compared to the other components, which is due to the fact that part of silica forms a liquid phase sintering process, lowering the

sintering temperature. The dielectric properties of the SCT core are strongly related to the sintering temperature and high sintering temperature helps to improve the dielectric permittivity²⁷. When the coating amount exceeds 3wt%, the permittivity decreases with an increasing amount of coating, which is due to increase of silica volume fraction. Different core materials affect the dielectric properties significantly. For example, SCT@3wt% SiO₂ has a much higher permittivity than ST@3wt% SiO₂ ($\epsilon_r \sim 247$ @1kHz) at room temperature, it also has a wider temperature stability range, enlarging the temperature range from 230 to 390°C whilst maintaining temperature coefficient of capacitance (TCC) $\leq \pm 15\%$. All the compositions exhibit thermal dielectric stability in a wide temperature range. Especially for the SCT@1wt% SiO₂ sample, an almost linear dependence with temperature is exhibited from room temperature to 500°C. This leads to TCC $\leq \pm 15\%$ for that temperature range.

Dielectric loss of SCT@1wt% SiO₂ samples are less than 3% at room temperature and 1k Hz, and other SCT@xwt% SiO₂ components can also maintain a low dielectric loss (< 0.1) in the same conditions. The dielectric loss increases with thicker coatings, which is attributed to the complexity of the system due to the increased defects introduced by silica. The effect of different core materials on the dielectric loss properties is also evident. The dielectric loss of SCT@3wt% SiO₂ is lower than ST@3wt% SiO₂, and has a suppressed dielectric relaxation peak at 250°C. In conclusion, SCT@3wt% SiO₂ compared to ST@3wt% SiO₂ exhibited a flatter dielectric loss and wider dielectric stability temperature range. Rare earth element doping not only plays an important role in improving the dielectric properties but can also enhance the thermo-dielectric stability which is related to the donor doped SrTiO₃ and formation of defect and defect clusters suppressing the motion and ionization of oxygen vacancies^{27, 40, 41}.

Table 2. Room temperature dielectric permittivity (1k Hz) SCT@xwt% SiO₂ (x=1.0, 3.0, 5.0, 7.0) and ST@3wt% SiO₂ at different sintered temperature.

Sintering temperature	SCT@1.0wt% SiO ₂	SCT@3.0wt% SiO ₂	SCT@5.0wt% SiO ₂	SCT@7.0wt% SiO ₂	ST@3.0wt% SiO ₂
1280°C	258	323	211	208	241
1300°C	373	615	347	260	247
1325°C	958	602	432	284	242

Table 2 shows the dielectric permittivity for each sample, sintered at different temperatures (1280°C, 1300°C and 1325°C). The dielectric permittivity initially increased as the amount of SiO₂ increased from 1wt% to 3wt% and then decreased with the continuous increase of SiO₂ content. The maximum dielectric constant reached $\epsilon_r \sim 615$ at SCT@3wt% SiO₂ (sintered at 1300°C). Increasing the sintering temperature can improve the dielectric permittivity, but the breakdown strength was significantly decreased. The sintering temperature of the sample is positively correlated with the dielectric permittivity owing to higher temperatures during processing leading to more defects introduced into the system²⁷. Thus, with the appropriate amount of silica, the sintering temperature can be effectively reduced, such that the dielectric permittivity of the materials can be closer to the pure core materials sintered at a higher temperature. However, generally speaking an increased

coating thickness reduces the effective permittivity.

Energy storage properties of SCT@SiO₂ ceramics

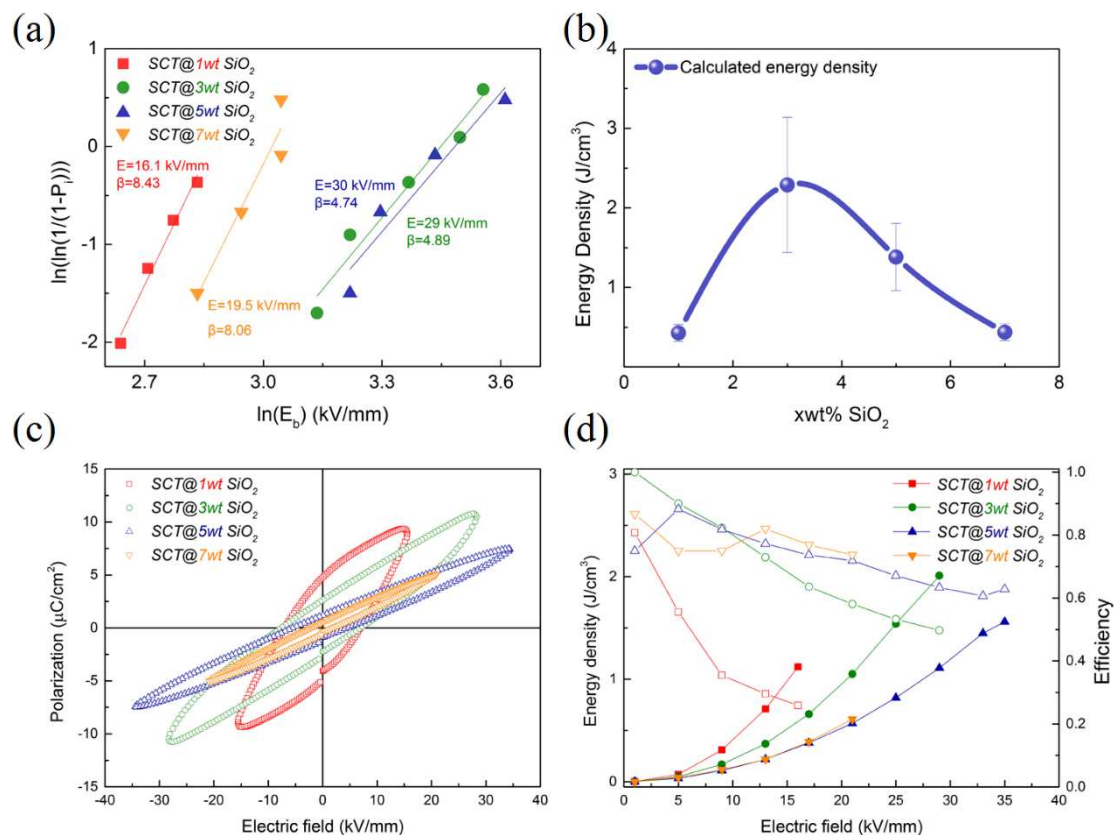


Figure 6. (a) Weibull distribution and deduced characteristic breakdown strength, (b) the experimental calculated energy density, (c) room temperature P-E hysteresis loops and (d) variation of the energy density (solid symbols, right Y axis) and discharge efficiency (hollow symbols, left Y axis) under various electric field of SCT@xwt% SiO₂ (x=1.0, 3.0, 5.0, 7.0). All samples were sintered at 1300°C.

The characteristic breakdown strength of different SCT@xwt%SiO₂ was analyzed using a Weibull distribution as shown in Fig. 6a. The greatly improved breakdown strength ~30 kV/mm could be achieved when x=5. The breakdown strength increases with the increase of the coating amount up to x=5, and then rapidly decreases when the coating amount above x=7. When the covering amount exceeds 5wt%, part of the silica may have other forms of uneven and complex components in the sample which makes the carrier concentration increase and breakdown strength decrease. In practice, we also found that when $x > 5$ wt%, the samples after sintering become more inhomogeneous. As energy storage properties of composites are dominated by the breakdown strength and dielectric properties, the variation in the trend of experimental calculated energy density using equation 2 with different SiO₂ coating amounts correlates with breakdown strength, as shown in Fig. 6b. The sample of x=3 sintered at 1300°C maintain a high dielectric permittivity and also has the largest energy storage density of ~2.23 J/cm³. The breakdown strength initially increased with addition of SiO₂ but after about 5wt% SiO₂ declines. That may due to the

difference in melting point of core and shell material, higher SiO₂ amount will produce more porosity resulting in decreased breakdown strength. Combined with previous morphological and phase analysis, SiO₂ can improve the breakdown strength ascribing to small grain sizes and high resistivity of SiO₂ coating layer. The P-E loops of different SCT@xwt%SiO₂ measured at room temperature and under their breakdown electric field are shown in Fig. 6c and the results of calculating energy storage efficiency by integral area are shown in the Fig. 6d. It is found that the SCT@3wt% SiO₂ composition exhibits a maximum polarization (P_{max}) of $\sim 10.8 \mu\text{C}/\text{cm}^2$ and with increasing SiO₂ coating content P_{max} decreases to $\sim 7.5 \mu\text{C}/\text{cm}^2$ for $x=5$ and to $\sim 5.1 \mu\text{C}/\text{cm}^2$ for $x=7$, due to the limitation of lower breakdown strength. However, the energy storage efficiency is increased with increasing SiO₂ coating content. Although lower SiO₂ coating content ($x=1, 3 \text{ wt}\%$) exhibits higher polarization than that of higher coating content ($x=5, 7 \text{ wt}\%$) samples, at low electric fields, the leakage current increase with increasing electric field, leading to the decrease of energy storage efficiency.

Finite element simulations

Having found superior properties in the 3wt% SiO₂ composition, FEM simulations were used to further study this configuration. The grain size was set to be approximately 4-5 μm to mimic the microstructure of the 3wt% composition (see Fig. 7a). Core volume fractions ranging from 0.700 to 0.985 were simulated. Firstly, DC simulations were used to find the electric field and current density distributions. Both the electric field and current density were found to be concentrated in the shell material in series to the applied voltage (see the horizontal lines of high field and current in Figs. b and c respectively).

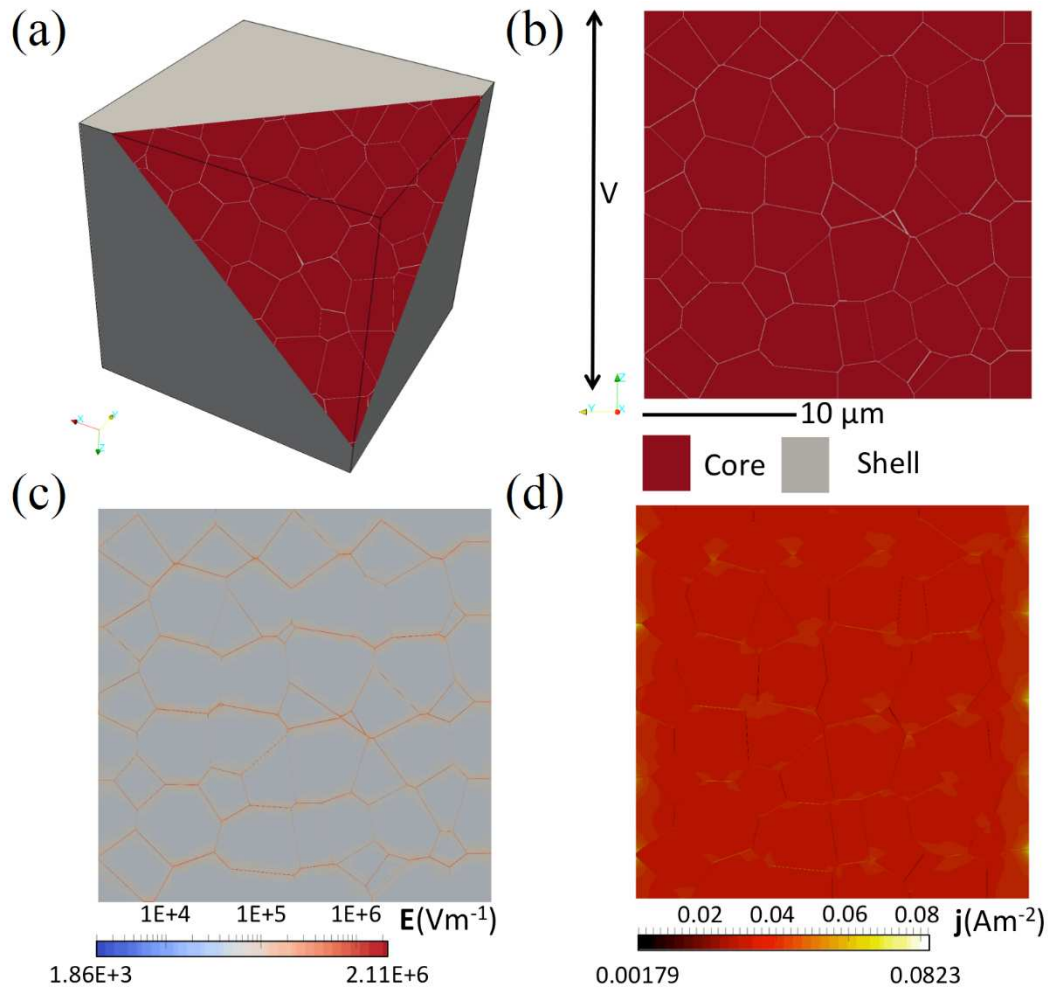


Fig. 7. (a) 3D model geometry of 0.98 core volume fraction with top corner removed to visualize the core-shell microstructure within. (a) Cross sections of simulation geometry for a core volume fraction of 0.98: (b) distribution of simulated microstructure, (c) electric field distribution and (d) current density distribution. Note all plots (b-d) are from the same cross section and the scale of (b) is logarithmic.

The electric field distributions for the SCT simulations were also quantitatively analyzed. For all volume fractions the maximum field was greater in the shell than in the core (see fig. S1). Generally, the maximum field increased with core volume fraction but there was scatter in the results even after averaging over three microstructural configurations. The minimum field strength in the core was always greater than that in the shell (see fig. S1). The minimum field in the core increased non-linearly with core volume fraction. For the shell the minimum field increased up to a core volume fraction of 0.85 then decreased non-linearly with core volume fraction.

Bounds for the breakdown strength of the simulated composite were calculated as detailed in the finite element methodology section. The lower bounds were calculated from the maximum field strength in the core and shell and decreased with core volume fraction (see fig. S2). There was significant scatter as would be expected from the scatter in the maximum field results (fig. S1). All the breakdown strength values calculated for the core volume fraction range were significantly below the

measured 3wt% SiO₂ value of 29 kV/mm and the value for SCT on its own, 20 kV/mm. Conversely the upper bound of breakdown strength predicted from the minimum field in the shell material was at one to two orders of magnitude greater than the breakdown strength of the 3wt% composition (see fig. S2). This was also higher than the shell material in isolation (60 kV/mm).

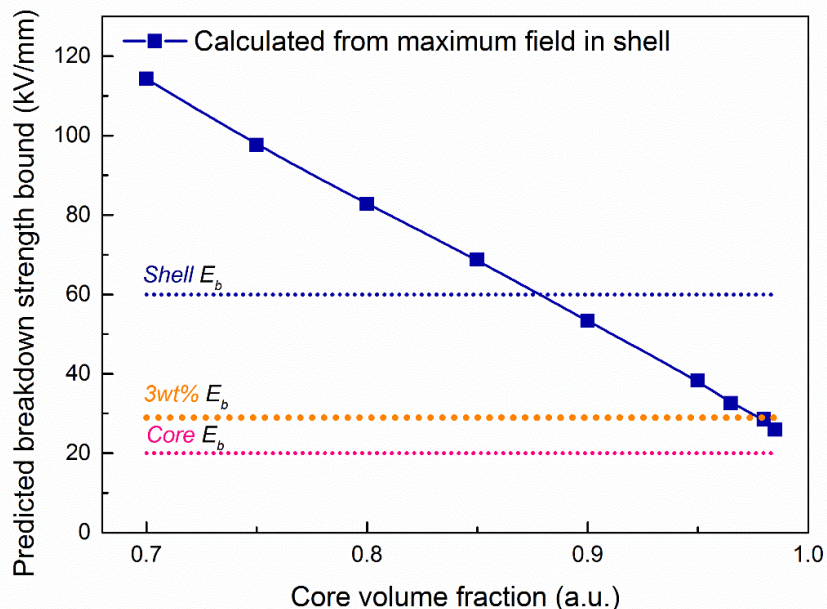


Figure. 8. Predicted upper bound of composite breakdown strength calculated from the minimum field values in the core material. Note the dotted lines indicate the experimentally measured breakdown strength of the core, shell and 3wt% materials. The line is a guide for the eye.

The upper bound of composite breakdown strength predicted using the minimum core field strength decreased with core volume fraction (see fig. 8). However, the values for large core volume fraction (~ 0.95) are close to the measured breakdown strength of the 3wt% composition. A core volume fraction of 0.98 best matched the experimental value of 29 kV/mm with 28.5 kV/mm. The simulated core volume fraction of 0.98 has a good agreement with the 3wt% coating composition (theoretical core volume fraction of 0.978) and so the breakdown strengths predicted for the minimum core field strength were used to calculate breakdown strength for the other core volume fractions simulated. Breakdown strength decreased as the core volume fraction increased (see fig. 9).

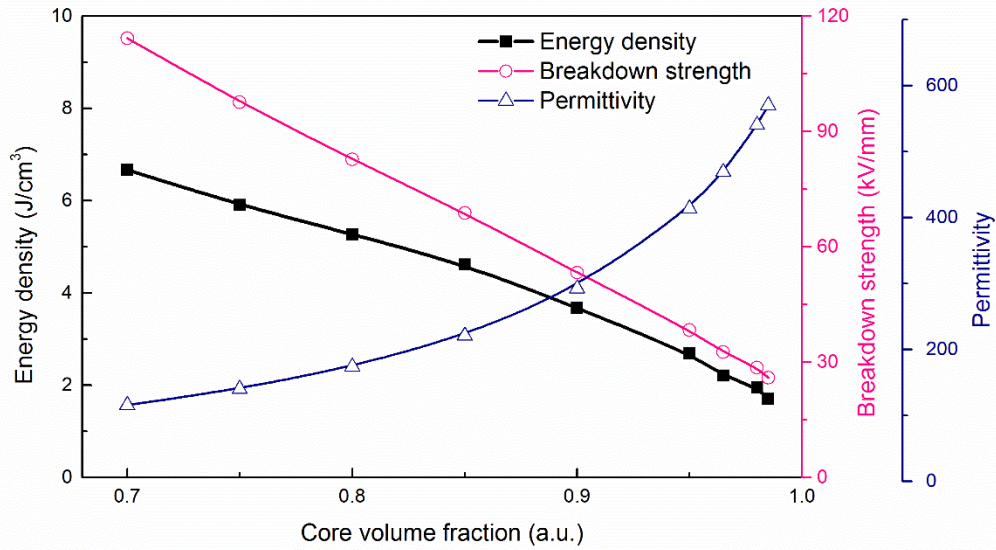


Figure. 9 Predicted breakdown strength (black), permittivity (pink) and energy density (blue) for simulated SCT microstructures versus volume fraction.

Table. 3. Comparison of experimental and modeling results with best agreement for the 3wt% composition.

	U/Jcm^{-3}	ϵ_r/au	$E/kVmm^{-1}$
Model	1.95	540.7	28.5
Experimental	~2.23	615	29.0

An AC simulation of each volume fraction allowed the permittivity at 100 Hz to be calculated. Fig. 9. Shows the permittivity of the composites increasing with core volume fraction. Using the predicted breakdown strengths and simulated permittivity values it is possible to calculate the energy density of the simulated composites. The energy density decreased as core volume fraction increased. Again, the 0.98 core volume fraction had the values of permittivity and energy density that were closest to the experimentally observed values for the 3wt% composition. A comparison of the simulate 0.98 and experimental 3wt% composition is given in table 3.

It is interesting that the model slightly under estimates energy density, permittivity and breakdown strength. We suspect that the permittivity values inputted into the model is lower than in reality since we did not consider the effect of porosity³⁶, internal barrier layer capacitor effect (IBLC)⁴², surface barrier capacitor effect (SBLC)⁴³ and chemical defect effect during the sintering process²⁷. Nevertheless, the output values agree well with experimental values. It is clear from the higher electric field and current density in the shell material that the presence of the shell greatly contributes to the electrical response of the composite. A change in electric field strength distributed at the interface between the insulating layer and inside grain causes the insulating shell layer to experience a higher current density and electric

field, which increase its contribution for the improvement of breakdown strength. However, predicted breakdown strengths imply that it is the reduction of field strength in the core that increases the breakdown strength of the composite when compared to SCT in isolation. Hence the lower field in the core is more important in deriving the effective composite properties.

Conclusions

Following previous work, we selected Ce doped SrTiO₃ as the core and coated it with SiO₂ via the Stöber method to synthesize “core-shell” structured (SCT@SiO₂) particles. The thickness of shell can be controlled by the content of TEOS. The effective coating content is about 0~5wt% and the SiO₂ shell thickness can be controlled in range of 0~6 nm. Although, the shell became thicker with increasing SiO₂ amount, some SiO₂ exists in other forms. The effect of xwt% SiO₂ (x=1, 3, 5, 7) and sintering temperature on phase, microstructure, dielectric and breakdown strength were investigated. The breakdown strength is improved and the permittivity is reduced with increasing coating content. Increasing sintering temperature contributed to improve the permittivity but deteriorates the breakdown strength. The effect of different core materials on dielectric properties are also significant. SCT@3wt% SiO₂ compared to ST @3wt% SiO₂ exhibited a flatter dielectric loss and wider dielectric stability range. As a result, the SCT@3wt%SiO₂ ceramics sintered at 1300°C possess a high dielectric permittivity ($\epsilon_r \sim 615 @ 1\text{kHz}$) at room temperature, with breakdown strength of $\sim 29 \text{ kV/mm}$. The highest energy density for the SCT@3wt% SiO₂ is about 2.29 J/cm^3 . The significantly improved breakdown strength and energy density is due to a decrease in grain size and introduction of insulating material as shell layer.

Finite element modeling of the 3wt% SiO₂ SCT had good agreement with the experimental results for the 0.98 core volume fraction simulation. It is likely that the real material has a core volume fraction of ~ 0.98 . Current density and electric field plots of the simulated microstructures show the effect of the shell shielding the core from higher currents and field strengths. Since the SCT core is the weakest component of the system, in terms of breakdown strength, reduced field in the core results in a significant increase in breakdown strength. This study has revealed the critical role of the electric field distribution on the breakdown strength and energy storage properties in core-shell materials, providing a possible method to achieve high energy storage application using a two phase composite material.

Acknowledgements

This work was supported by NSFC-Guangdong Joint Funds of the Natural Science Foundation of China (No.U1601209), Major Program of the Natural Science Foundation of China (51790490), the National Key Basic Research Program of China (973 Program) (No. 2015CB654601) and Technical Innovation Special Program of Hubei Province (2017AHB055). We also thank the Engineering and Physical Science

Research Council (EPSRC) for funding through EP/L017563/1 and EP/P019919/1 in relation to the finite element modelling shown.

References

1. Z. H. Yao, Z. Song, H. Hao, Z. Y. Yu, M. H. Cao, S. J. Zhang, M. T. Lanagan and H. X. Liu, *Adv Mater*, 2017, **29**.
 2. C. C. Homes, T. Vogt, S. M. Shapiro, S. Wakimoto and A. P. Ramirez, *Science*, 2001, **293**, 673-676.
 3. S. Krohns, P. Lunkenheimer, S. Meissner, A. Reller, B. Gleich, A. Rathgeber, T. Gaugler, H. U. Buhl, D. C. Sinclair and A. Loidl, *Nature materials*, 2011, **10**, 899-901.
 4. H. B. Lu, G. Z. Yang, Z. H. Chen, S. Y. Dai, Y. L. Zhou, K. J. Jin, B. L. Cheng, M. He, L. F. Liu, H. Z. Guo, Y. Y. Fei, W. F. Xiang and L. Yan, *Appl Phys Lett*, 2004, **84**, 5007-5009.
 5. G. Subodh, J. James, M. T. Sebastian, R. Paniago, A. Dias and R. L. Moreira, *Chem Mater*, 2007, **19**, 4077-4082.
 6. G. Y. Li, H. X. Liu, H. Hao, J. J. Liu, Z. Chen, X. D. Huang, M. H. Cao and Z. H. Yao, *Ceram Int*, 2016, **42**, 16782-16788.
 7. J. Wu, C. W. Nan, Y. Lin and Y. Deng, *Phys Rev Lett*, 2002, **89**, 217601.
 8. Y. Q. Wu, X. Zhao, J. L. Zhang, W. B. Su and J. Liu, *Appl Phys Lett*, 2015, **107**.
 9. Q. Li, L. Chen, M. R. Gadinski, S. Zhang, G. Zhang, U. Li, E. Iagodkine, A. Haque, L. Q. Chen, N. Jackson and Q. Wang,
-

-
- Nature*, 2015, **523**, 576-579.
10. L. Zhao, Q. Liu, J. Gao, S. J. Zhang and J. F. Li, *Adv Mater*, 2017, **29**.
 11. Q. Li, K. Han, M. R. Gadinski, G. Z. Zhang and Q. Wang, *Adv Mater*, 2014, **26**, 6244-6249.
 12. X. Zhang, Y. Shen, B. Xu, Q. H. Zhang, L. Gu, J. Y. Jiang, J. Ma, Y. H. Lin and C. W. Nan, *Adv Mater*, 2016, **28**, 2055-+.
 13. Y. F. Wang, J. Cui, L. X. Wang, Q. B. Yuan, Y. J. Niu, J. Chen, Q. Wang and H. Wang, *J Mater Chem A*, 2017, **5**, 4710-4718.
 14. L. Y. Xie, X. Y. Huang, C. Wu and P. K. Jiang, *J Mater Chem*, 2011, **21**, 5897-5906.
 15. L. W. Wu, X. H. Wang, H. L. Gong, Y. N. Hao, Z. B. Shen and L. T. Li, *J Mater Chem C*, 2015, **3**, 750-758.
 16. C. L. Diao, H. X. Liu, H. Hao, M. H. Cao and Z. H. Yao, *Ceramics International*, 2016, **42**, 12639-12643.
 17. V. K. Deshpande and M. V. Jagdale, *Ferroelectrics*, 2017, **510**, 95-102.
 18. Y. C. Lee, W. H. Lu, S. H. Wang and C. W. Lin, *Int J Min Met Mater*, 2009, **16**, 124-127.
 19. S. F. Wang, S. J. Wang, Y. R. Wang, Y. F. Hsu, L. Y. Chen and
-

-
- J. S. Tsai, *Ceramics International*, 2009, **35**, 1813-1817.
20. P. Gao, H. M. Ji, Q. Q. Jia and X. L. Li, *J Alloy Compd*, 2012, **527**, 90-95.
21. F. Z. Zeng, M. H. Cao, L. Zhang, M. Liu, H. Hao, Z. H. Yao and H. X. Liu, *Ceramics International*, 2017, **43**, 7710-7716.
22. R. Ma, B. Cui, M. Shangguan, S. H. Wang, Y. J. Wang, Z. G. Chang and Y. Y. Wang, *J Alloy Compd*, 2017, **690**, 438-445.
23. Y. C. Zhang, X. H. Wang, J. Y. Kim, Z. B. Tian, J. Fang, K. H. Hur and L. T. Li, *J Am Ceram Soc*, 2012, **95**, 1628-1633.
24. S. Mornet, C. Elissalde, V. Hornebecq, O. Bidault, E. Duguet, A. Brisson and M. Maglione, *Chem Mater*, 2005, **17**, 4530-4536.
25. F. Li, D. B. Lin, Z. B. Chen, Z. X. Cheng, J. L. Wang, C. C. Li, Z. Xu, Q. W. Huang, X. Z. Liao, L. Q. Chen, T. R. ShROUT and S. J. Zhang, *Nature materials*, 2018, **17**, 349-+.
26. A. Mukherjee, S. Basu, P. K. Manna, S. M. Yusuf and M. Pal, *J Mater Chem C*, 2014, **2**, 5885-5891.
27. J. L. Qi, M. H. Cao, Y. Y. Chen, Y. Fang, W. G. Pan, H. Hao, Z. H. Yao, Z. Y. Yu and H. X. Liu, *J Alloy Compd*, 2018, **762**, 950-956.
-

-
28. H. J. Zhang, H. M. Xiong, Q. G. Ren, Y. Y. Xia and J. L. Kong, *J Mater Chem*, 2012, **22**, 13159-13165.
 29. J. S. Dean, J. H. Harding and D. C. Sinclair, *J Am Ceram Soc*, 2014, **97**, 885-891.
 30. J. P. Heath, J. S. Dean, J. H. Harding and D. C. Sinclair, *J Am Ceram Soc*, 2015, **98**, 1925-1931.
 31. J. S. Dean, P. Y. Foeller, I. M. Reaney and D. C. Sinclair, *J Mater Chem A*, 2016, **4**, 6896-6901.
 32. P. Y. Foeller, J. S. Dean, I. M. Reaney and D. C. Sinclair, *Appl Phys Lett*, 2016, **109**.
 33. M. Tanemura, T. Ogawa and N. Ogita, *Journal of Computational Physics*, 1983, **51**, 191-207.
 34. A. R. West, D. C. Sinclair and N. Hirose, *J Electroceram*, 1997, **1**, 65-71.
 35. Z. M. Cai, X. H. Wang, B. C. Luo, W. Hong, L. W. Wu and L. T. Li, *J Am Ceram Soc*, 2018, **101**, 1607-1615.
 36. G. Dale, M. Strawhorne, D. C. Sinclair and J. S. Dean, *J Am Ceram Soc*, 2018, **101**, 1211-1220.
 37. R. Ubic, G. Subodh, D. Gout, M. T. Sebastian and T. Proffen, *Chem Mater*, 2009, **21**, 4706-4710.
 38. R. Ubic, G. Subodh, M. T. Sebastian, D. Gout and T. Proffen, *Chem Mater*, 2008, **20**, 3127-3133.
-

-
39. Y. M. Zhang, M. H. Cao, Z. H. Yao, Z. J. Wang, Z. Song, A. Ullah, H. Hao and H. X. Liu, *Mater Res Bull*, 2015, **67**, 70-76.
 40. Z. C. He, M. H. Cao, L. Zhou, L. Zhang, J. Xie, S. J. Zhang, J. L. Qi, H. Hao, Z. H. Yao, Z. Y. Yu and H. X. Liu, *Journal of American Ceramic Society*, 2018, **00**, 1-9.
 41. P. R. L. Keating, D. O. Scanlon and G. W. Watson, *J Mater Chem C*, 2013, **1**, 1093-1098.
 42. M. Fujimoto and W. D. Kingery, *Journal of American Ceramic Society*, 2010, **68**.
 43. C. C. Wang, C. M. Lei, G. J. Wang, X. H. Sun, T. Li, S. G. Huang, H. Wang and Y. D. Li, *J Appl Phys*, 2013, **113**.
-